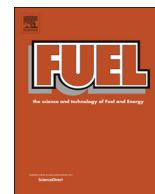




ELSEVIER

Contents lists available at ScienceDirect

Fuel

journal homepage: [www.elsevier.com/locate/fuel](http://www.elsevier.com/locate/fuel)

Full Length Article

# Modelling *n*-heptane dilute spray flames in a model supersonic combustor fueled by hydrogen

Zhiwei Huang, Majie Zhao, Huangwei Zhang\*

Department of Mechanical Engineering, National University of Singapore, 9 Engineering Drive 1, Singapore 117576, Republic of Singapore

## ARTICLE INFO

## Keywords:

*n*-Heptane spray flame  
Dual fuel  
Flame stabilization  
Droplet evaporation  
Reactant mixing  
Supersonic combustion

## ABSTRACT

Combustion characteristics of *n*-heptane dilute sprays in a model supersonic combustor fueled by hydrogen are numerically investigated. The two-phase compressible reactive flows are solved by a Eulerian-Lagrangian framework. Supersonic air enters the combustor at Mach 2.0, whereas hydrogen is injected sonically at the strut base. Monodispersed liquid *n*-heptane droplets are carried by hydrogen jet at different Spray Equivalence Ratios (SERs), which range from 0 to 0.096. The results show that the varied SERs negligibly influence the time-averaged length of the recirculation zone (about 50 mm off the rear of the strut). However, the low-speed regions in the combustor is increased with SER. High droplet evaporation rates are observable in the downstream of the recirculation zone, and meanwhile continuous evaporation also occurs downstream beyond that due to the local high temperature. The mixing field of the dual-fuel system shows strong inhomogeneity with various compositions of hydrogen/*n*-heptane/air mixtures in both mixture fraction space and physical space. Moreover, the fraction of heat release rate from hydrogen decreases from 100% to 43.3% due to the increased SERs from 0 to 0.096, and the averaged heat release from hydrogen before blow-off are close, whereas that from *n*-heptane increases stably. With increased SER, the hydrogen flame base moves upstream towards the strut base, whereas that of *n*-heptane is lifted off the strut gradually. When SER exceeds some critical value, e.g. 0.096 for the current combustor, the flame blows off, with the two separate reaction zones (upstream hydrogen and downstream *n*-heptane) fully quenched.

## 1. Introduction

Liquid hydrocarbon fuels (LHCFs) have several advantages over gaseous fuels, e.g. hydrogen (H<sub>2</sub>) and ethylene, in terms of easy storage and the potential of being coolant in supersonic combustion ramjets (scramjets) or scramjet-based combined-cycle engines [1,2]. However, generally very complex physical-chemical processes, such as injection, atomization, droplet breakup, evaporation, mixing, ignition, and flame stabilization are involved in combustion of LHCFs in practical hypersonic propulsion systems. Stable combustion is a great challenge in scramjet-like combustors due to the high-speed incoming flows, in which case the gas residence time is of the order of milliseconds [3]. In such a short time, the injected LHCFs have to be atomized, evaporated, and well mixed before combustion of the fuel vapor can occur in the high-speed flows [4].

Kumaran et al. [5] investigated the supersonic kerosene combustion in three model combustors with single-step chemistry using Reynolds-Averaged Navier-Stokes method. It was found that the mixing process

plays an important role in heat release and thrust generation. Zhang et al. [6] numerically studied the spray kerosene combustion in a model supersonic combustor with cavity flame holder using four-step global mechanism. The flow structures in the cavity were found to be important for the spray distribution and the resulted combustion performance. Tian et al. [7] experimentally and numerically studied the combustion performance of a kerosene-fueled dual-mode scramjet, in which the effects of Spray Equivalence Ratio (SER) and fuel distribution were examined. Flame stabilization of a hydrogen and kerosene fueled combustor was also investigated by Tian et al. [8], and it was found that the local SER considerably affects combustion stability. There are also experimental studies on supersonic spray combustion of LHCFs [9–12]. However, most of these studies focused on the overall indices with limited measurement data attainable, e.g. combustion efficiency and engine performance, which is certainly of great importance for practical engineering applications. Nevertheless, the fundamental aspects of spray combustion under high-speed flow conditions have not been well understood. The basic questions in supersonic spray combustion

\* Corresponding author at: Department of Mechanical Engineering, Faculty of Engineering, National University of Singapore, 9 Engineering Drive 1, Singapore 117576, Republic of Singapore.

E-mail addresses: [mpehuan@nus.edu.sg](mailto:mpehuan@nus.edu.sg) (Z. Huang), [huangwei.zhang@nus.edu.sg](mailto:huangwei.zhang@nus.edu.sg) (H. Zhang).

<https://doi.org/10.1016/j.fuel.2019.116809>

Received 13 September 2019; Received in revised form 24 November 2019; Accepted 2 December 2019

0016-2361/© 2019 Elsevier Ltd. All rights reserved.

## Nomenclature

### Symbols

$\rho_g$	density of the gas
$p_g$	pressure of the gas
$T_g$	temperature of the gas
$u_{j,g}$	velocity of the gas in $j$ -th direction
$e_g$	internal energy of the gas
$c_{p,g}$	heat capacity of the gas
$\mu_g$	dynamic viscosity of the gas
$D_g$	molecular diffusion coefficient
$Sc$	Schmidt number
$Pr$	Prandtl number
$k_g$	thermal conductivity of the gas
$\tau_{ij}$	viscous stress tensor
$\delta_{ij}$	unit tensor function
$q$	heat flux
$Y_m$	mass fraction of species $m$
$\dot{\omega}_m$	reaction rate of species $m$
$S_m$	mass source term from droplet
$S_{i,F}$	momentum source term from droplet
$S_e$	energy source term from droplet
$S_{Y,m}$	species source term from droplet
$V_c$	volume of the CFD cell
$N_d$	number of droplets in a CFD cell
$\rho_d$	density of the droplet
$m_d$	mass of the droplet
$T_d$	temperature of the droplet
$F_{i,d}$	drag force acting on the droplet in $i$ -th direction
$d_d$	diameter of the droplet
$A_d$	surface area of the droplet
$U_{slip}$	slip velocity between gas and droplet
$C_v$	evaporation coefficient
$M_d$	molecular weight of the vapor
$c_{p,d}$	heat capacity of the droplet
$u_{j,d}$	velocity component of the droplet
$h_c$	convective heat transfer coefficient
$\dot{m}_d$	evaporation rate of a single droplet

$\dot{Q}_c$	convective heat transfer rate of droplet
$Q_{lat}$	latent heat of evaporation of droplet
$\dot{m}_f$	mass flux of vapor through droplet surface
$k_c$	mass transfer coefficient
$c_s$	vapor concentration at droplet surface
$c_g$	vapor concentration in the gas
$p_{sat}$	saturated pressure of the droplet
$R_g$	universal gas constant
$X_i$	mole fraction of vapor in the gas
$Re_d$	droplet Reynolds number
$C_d$	coefficient of dynamic drag
$A$	frequency factor of chemical reactions
$n$	temperature exponent
$E_a$	activation energy
$a, b$	reaction orders
$\bar{S}_m$	averaged evaporation rate
$L_y$	vertical line perpendicular to $x$ -axis
$\xi_1, \xi_2$	a parameter set of mixture fraction
$dQ$	heat release rate per unit volume
$Z_F^{st}$	stoichiometric mixture fraction
$Q_i$	the volume-integrated heat release from fuel $i$ ( $H_2/n$ - $C_7H_{16}$ )
$f_{n-C_7H_{16}}$	fraction of heat release from $n$ -heptane
$d_{lift}$	flame lift-off height
$\epsilon_e$	relative error of $C_v$ to the experiment
min	minimum function

### Acronym

LHCF	liquid hydrocarbon fuel
SER	spray equivalence ratio
RZ	recirculation zone
CFD	computational fluid dynamics
3D	three-dimensional
2D	two-dimensional
LES	large eddy simulation
CFL	Courant-Friedrichs-Lewy
NTC	negative temperature coefficient

include: e.g. (1) how do the droplets evaporate and exchange heat with the high-speed gas flows? (2) How do the vaporized fuel species mix with the supersonic oxidizer flows? (3) How would the flame respond to the varied mass flow rates of liquid and/or gaseous fuels?

In recent years, Ren et al. performed a series of numerical simulations on the interactions of vortex, shock waves, and chemical reactions in a supersonic planar shear layer laden with liquid kerosene droplets [1,13,14]. It was concluded that the growth of mixing layer thickness, flame structure, and reaction intensity are affected by the competition between cooling from droplet evaporation and heat release from chemical reaction. Their work provides significant insights about the spray combustion under high-speed flow conditions. However, the modeled planar shear layer in open space is still different from practical supersonic combustor configurations. For instance, in the latter, the flow and combustion occur in a confined space, in which there are probably new aerodynamic characteristics not present in the simplified geometries. Furthermore, shock waves may be continuously reflected by the chamber walls and therefore may interact with the dispersed liquid droplets and the flame zones. The expansion wave may also influence the motion and evaporation of the droplets in the combustion chamber. Therefore, spray flame dynamics relevant to practical supersonic combustion conditions is still not clear.

The objective of our work is to investigate the dilute spray combustion characteristics of LHCFs in a model supersonic combustor. This

combustor was experimentally studied at the German Aerospace Center (DLR) with gaseous hydrogen flames [15]. Hereafter, we term this burner as DLR combustor. The main aerodynamic and combustion features of the  $H_2$ -fueled supersonic combustion in this burner include a long central Recirculation Zone (RZ), a lifted recirculating flame (a time-averaged lift-off distance of 31 mm off the strut base), and the shock-flame interactions [16]. The gaseous  $H_2$  flames in this combustor have been studied experimentally by Waidmann et al. [15] and numerically by numerous groups, e.g. Huang [17–19], Fureby [20,21], Menon [22], Gong [23], Li [24], Wang [25], and Wu [26]. Therefore, we have detailed understanding about them in terms of critical flame phenomena and numerical set-up. Based on this well-recognized configuration, in our numerical studies, liquid  $n$ -heptane ( $n$ - $C_7H_{16}$ ) spray injection is introduced in this combustor. The emphasis is laid on (1) the interactions between the liquid droplets and the high-speed gas flow; (2) the mixing between the two fuels ( $H_2$  and  $n$ - $C_7H_{16}$ ) and air; and (3) the influence of  $n$ -heptane droplets on the critical flame dynamics (e.g. lift-off or blow-off). For this purpose, eight numerical experiments with gradually increased spray equivalence ratio are conducted, which ranges from 0 (gaseous  $H_2$  flame without liquid spray) to 0.096 (the upper limit before flame blow-off occurs). The current investigation aims to clarify some aspects of our fundamental understanding on high-speed, two-phase, and dual-fuel combustion relevant to practical model supersonic combustor conditions. The rest of the

paper is structured as below. Governing equations and numerical models are described in Section 2. Physical models, including the computational configuration, meshes, and the simulation conditions are given in Section 3. The results and discussion are provided in Section 4. Conclusions are drawn in Section 5.

## 2. Governing equations and numerical models

### 2.1. Governing equations for gas phase

The governing equations for fully compressible multi-component reacting flows in gas phase include the conservation laws of mass, momentum, energy, and species mass fraction [27]. They read

$$\frac{\partial \rho_g}{\partial t} + \frac{\partial}{\partial x_j} (\rho_g u_{j,g}) = S_m, \quad (1)$$

$$\frac{\partial}{\partial t} (\rho_g u_{i,g}) + \frac{\partial}{\partial x_j} (\rho_g u_{i,g} u_{j,g} + p_g \delta_{ij} - \tau_{ij}) = S_{i,F}, \quad (2)$$

$$\frac{\partial}{\partial t} (\rho_g e_g) + \frac{\partial}{\partial x_j} (\rho_g e_g u_{j,g} + p_g u_{j,g} - q_j - u_{j,g} \tau_{ij}) = S_e, \quad (3)$$

$$\frac{\partial}{\partial t} (\rho_g Y_m) + \frac{\partial}{\partial x_j} (\rho_g Y_m u_{j,g}) - \frac{\partial}{\partial x_j} \left( \rho_g D_g \frac{\partial Y_m}{\partial x_j} \right) = \dot{\omega}_m + S_{Y,m}, \quad (4)$$

where  $t$  is time and  $x$  is spatial coordinate,  $\rho_g$  is the density of the gas mixture,  $u_{j,g}$  is the gas velocity component,  $p_g$  is the pressure,  $\tau_{ij}$  is the viscous stress tensor,  $\delta_{ij}$  is the unit tensor function,  $e_g$  is the internal energy of the gas,  $q_j$  is the heat flux,  $Y_m$  is the mass fraction of species  $m$ , and  $\dot{\omega}_m$  is the reaction rate of species  $m$ .  $D_g$  is the molecular diffusion coefficient and  $D_g = \rho_g \mu_g / Sc$ , where  $Sc$  is the Schmidt number,  $\mu_g$  is the dynamic viscosity of the gas. Two-way coupling between the gas phase and liquid phase is applied, in terms of the inter-phasic exchanges of mass, momentum, energy and species, which respectively correspond to the source terms  $S_m$ ,  $S_{i,F}$ ,  $S_e$ , and  $S_{Y,m}$  in Eqs. (1)–(4). These terms can be estimated on the droplets in the individual CFD cells, which read

$$S_m = \frac{1}{V_c} \sum_1^{N_d} \dot{m}_d, \quad (5)$$

$$S_{i,F} = -\frac{1}{V_c} \sum_1^{N_d} F_{i,d}, \quad (6)$$

$$S_e = -\frac{1}{V_c} \sum_1^{N_d} (\dot{Q}_c + \dot{Q}_{lat}), \quad (7)$$

$$S_{Y,m} = \begin{cases} S_m & \text{for the liquid fuel species,} \\ 0 & \text{for other species.} \end{cases} \quad (8)$$

here  $V_c$  is volume of the CFD cell,  $N_d$  is the droplet number in the cell,  $\dot{m}_d$  is the evaporation rate of single droplet and is given later in Eq. (14),  $F_{i,d}$  is the drag force acting on the droplet in  $i$ -th direction,  $\dot{Q}_c$  is the convective heat transfer rate between the droplet phase and gas phase and the corresponding equation is given in Eq. (22),  $\dot{Q}_{lat}$  is the evaporation-induced heat transfer, related to latent heat of vaporization for liquid  $n$ -heptane. Note that for Eq. (6), other forces (e.g. gravity and Magnus lift force) are not taken into consideration in the current work. Additionally, radiation heat transfer due to the gas and droplet phases is not included here.

### 2.2. Governing equations for liquid droplet phase

The dispersed liquid phase is modeled as a large number of spherical droplets tracked by the Lagrangian method. The interactions between droplets are neglected since dilute sprays are assumed here, in which the volume fraction of the dispersed droplet phase is typically less than 0.001 [28]. The shock-induced droplet break-up is not considered here. The governing equations of mass, momentum and energy for the liquid

droplet phase respectively take the following form

$$\frac{dm_d}{dt} = \dot{m}_d, \quad (9)$$

$$\frac{du_{i,d}}{dt} = \frac{F_{i,d}}{m_d}, \quad (10)$$

$$c_{p,d} \frac{dT_d}{dt} = \frac{\dot{Q}_c + \dot{Q}_{lat}}{m_d}, \quad (11)$$

where  $m_d$  is the mass of a single droplet and can be calculated as  $m_d = \pi \rho_d d_d^3 / 6$  for spherical droplets ( $\rho_d$  and  $d_d$  are the density and diameter of the droplet, respectively).  $u_{i,d}$  is the velocity component of droplet in  $i$ -th direction,  $c_{p,d}$  is the droplet heat capacity, and  $T_d$  is the droplet temperature. Both density and heat capacity of the droplet phase are functions of droplet temperature to account for the droplet thermal expansion [29]

$$\rho_d(T_d) = \frac{a_1}{a_2^{1+(1-T_d/a_3)^{a_4}}}, \quad (12)$$

$$c_{p,d}(T_d) = \frac{b_1^2}{\tau} + b_2 - \tau \left\{ 2.0b_1b_3 + \tau \left[ b_1b_4 + \tau \left[ \frac{1}{3}b_3^2 + \tau \left( \frac{1}{2}b_3b_4 + \frac{1}{5}\tau b_4^2 \right) \right] \right] \right\}, \quad (13)$$

where  $a_1$ ,  $a_2$ ,  $a_3$ ,  $a_4$ , and  $b_1$ ,  $b_2$ ,  $b_3$ ,  $b_4$ , are model constants,  $\tau = 1.0 - T/T_0$  with  $T = \min(T_d, T_0)$ , where  $T_0$  is a reference temperature (540.2 K for  $n$ -heptane),  $\min$  is the minimum function [29].

The evaporation rate,  $\dot{m}_d$ , in Eqs. (5) and (9) is estimated through  $\dot{m}_d = -\dot{m}_f A_d$ , (14)

where  $A_d$  is the surface area of a single droplet. The mass flux of vapor evaporating from the droplet into the gas phase,  $\dot{m}_f$ , is calculated as [30,31]

$$\dot{m}_f = k_c M_d (c_s - c_g). \quad (15)$$

It should be highlighted that use of a classical model as above can reduce the chance to include more *ad hoc* assumptions and/or constants for droplet evaporation under complicated flow conditions, thereby decreasing the uncertainties for our analysis on supersonic spray flames. In Eq. (15),  $k_c$  is the mass transfer coefficient, while  $M_d$  is the molecular weight of the vapor.  $R_g$  ( $= 8.314$  J/mol·K) is the universal gas constant, and  $T_f$  is the film temperature, which is estimated using the two-third rule between the gas and droplet temperatures, i.e.  $T_f = (T_g + 2T_d)/3$  [31].  $c_s$  is the vapor concentration at the droplet surface, i.e.

$$c_s = \frac{p_{sat}(T_d)}{R_g T_f}, \quad (16)$$

where  $p_{sat}$  is the saturation pressure and is obtained under the assumption that the vapor pressure at the droplet surface is equal to that of the gas phase. In Eq. (15), the vapor concentration in the surrounding gas,  $c_g$ , is obtained from

$$c_g = \frac{p_g X_i}{R_g T_f}, \quad (17)$$

where  $X_i$  is the fuel vapor mole fraction. The mass transfer coefficient,  $k_c$ , in Eq. (15) is calculated from the Sherwood number [32]

$$Sh_{ab} = \frac{k_c d_d}{D_f} = 2.0 + 0.6 Re_d^{1/2} Sc^{1/3}, \quad (18)$$

where  $D_f$  is the vapor mass diffusivity in the gas phase. The droplet Reynolds number in Eq. (18),  $Re_d$ , is defined based on the velocity difference between two phases, i.e.

$$Re_d \equiv \frac{\rho_d d_d |\vec{u}_d - \vec{u}_g|}{\mu_g} \quad (19)$$

Only the Stokes drag is taken into consideration in this work, which is modeled as (assuming that the droplet is spherical) [33]

$$F_{i,d} = \frac{18\mu_g C_d Re_d}{\rho_d d_d^2} m_d |u_{i,d} - u_{i,g}| \quad (20)$$

The drag coefficient,  $C_d$ , is estimated as [33]

$$C_d = \begin{cases} 0.424, & Re_d > 1000, \\ \frac{24}{Re_d} \left(1 + \frac{1}{6} Re_d^{2/3}\right), & Re_d < 1000. \end{cases} \quad (21)$$

The convective heat transfer rate  $\dot{Q}_c$  in Eq. (11) is given by

$$\dot{Q}_c = h_c A_d (T_g - T_d) \quad (22)$$

where  $h_c$  is the convective heat transfer coefficient, and computed using the correlation by Ranz and Marshall [32]

$$Nu = \frac{h_c d_d}{k_g} = 2.0 + 0.6 Re_d^{1/2} Pr^{1/3}, \quad (23)$$

where  $k_g$  is the gas thermal conductivity, and  $Pr$  is the gas Prandtl number ( $Pr = \mu_g c_{p,g} / k_g$ , where  $c_{p,g}$  is heat capacity of the gas phase).

### 2.3. Chemical kinetics

Two-step irreversible reactions, i.e. Reactions I and II in Table 1, are used for describing oxidization of *n*-heptane [34] and hydrogen [35]. The reaction steps with kinetics parameters for  $H_2/O_2$  and  $n-C_7H_{16}/O_2$  are listed in Table 1, including frequency factor  $A$ , temperature exponent  $n$ , activation energy  $E_a$ , and reaction orders  $a$  and  $b$  with respect to the corresponding reactants. The Arrhenius reaction rates for Reactions I and II are expressed as

$$\dot{\omega} = AT^n \exp\left(-\frac{E_a}{RT}\right) [F]^a [O]^b, \quad (24)$$

where  $[F]$  and  $[O]$  are the concentrations of the fuel and oxidizer, respectively.

The global reaction for  $H_2$ , i.e. Reaction I, has been validated with experimental data in terms of laminar flame speed, which shows good agreement for equivalence ratios ranging from 0.55 to 1.1 [35]. This mechanism has also been used by Ingenito et al. [36], Gerlinger et al. [37], and Fureby et al. [38] for modelling supersonic combustion and it is found that the main combustion characteristics (e.g. wall pressure and temperature predictions [36], laminar flame speed [37], and flame stabilization [38]) are captured well. Furthermore, compared with our previous investigations on this combustor using three-dimensional (3D) Large Eddy Simulation (LES) with detailed hydrogen chemistry of 9 species and 27 reactions [17–19], this global mechanism well reproduces the abovementioned main flow and combustion characteristics observed from experiments.

The one-step mechanism for  $n-C_7H_{16}$ , i.e. Reaction II, is validated by Westbrook et al. [34] about the laminar flame speed. The results show good agreement with the measured data over a range of pressures and equivalence ratios and also reasonably reproduce the rich and lean flammability limits [34]. The same mechanism is used, e.g. by Seo and Huh [39], Owston and Magi [40], Li and Huang [41] for modelling spray *n*-heptane flames. It has been found that this mechanism is

**Table 1**  
Chemical kinetics parameters for  $H_2/O_2$  and  $n-C_7H_{16}/O_2$  (units in cm-sec-mole-cal-Kelvins).

Index	Reaction	$A$	$n$	$E_a$	$a$	$b$	Reference
I	$2H_2 + O_2 = > 2H_2O$	$4.74 \times 10^{12}$	0.0	10,063.8	1.0	0.5	[35]
II	$n-C_7H_{16} + 11O_2 = > 7CO_2 + 8H_2O$	$5.10 \times 10^{11}$	0.0	30,000.0	0.25	1.5	[34]

sufficient to capture the general spray combustion characteristics of *n*-heptane under different conditions. In addition, it is well-known that the flame dynamics related to Negative Temperature Coefficient (NTC) may be important for hydrocarbon fuels (like *n*-heptane) under proper temperature ranges (e.g.  $< 1000$  K) [13,42]. However, in the cases studied here, the significant evaporation of the fuel droplets is observed to mainly occur at the downstream locations after the hydrogen flames (as shown later in Section 4), and therefore the fuel vapor combustion proceeds under high local temperatures ( $> 2000$  K). Therefore, the NTC effect is assumed to be not important in this work, and the global chemical reaction in Table 1 is expected to be sufficient.

### 2.4. Numerical methods

A two-phase multi-component reactive solver, *sprayRhoCentralFoam*, is developed based on a fully compressible flow solver *rhoCentralFoam* [43], in OpenFOAM 5.0 package. The *rhoCentralFoam* solver itself is a density-based compressible flow solver. It is able to capture shock waves with low dissipation by solving the convection-diffusion equations using the semi-discrete Kurganov-Tadmor central-upwind schemes [44,45]. This *rhoCentralFoam* solver has been validated with supersonic flows and detonative combustion [46]. It is also used by other groups, e.g. by Li et al. [24] and Wu et al. [26], for the supersonic  $H_2$  flames in the same DLR combustor, and good accuracies are achieved in terms of the velocity, pressure and overall flame behaviors.

The governing equations for gas phase (i.e. Eqs. (1)–(4)) are solved by cell-centered finite volume method. Implicit second-order Crank-Nicolson scheme is applied for the time discretization. Second-order Gauss integration with linear interpolation scheme is constructed for the convective fluxes. The diffusive terms are split into orthogonal part and non-orthogonal part to minimize the non-orthogonality error. Second-order Gauss scheme with a linear interpolation is used for the orthogonal part and surface interpolation of variable normal gradients is applied to the non-orthogonal part [47]. The Lagrangian governing equations (i.e. Eqs. (9)–(11)) for mass, velocity and temperature of each droplet are numerically integrated with Euler implicit method. The gas phase quantities at the droplet location (e.g.  $u_{i,g}$  in Eq. (18) and  $T_g$  in Eq. (20)) are linearly interpolated from the gas phase fields solved from Eqs. (1)–(4). Two-way coupling between two phases is performed for each time to update the source terms in the gas and droplet phase equations. The maximum CFL numbers are set to be 0.3, which corresponds to the physical time step of about  $10^{-9}$  s. The time-averaged fields shown below are computed in a period of 3.0 ms after the initial field effects are completely purged in each simulation.

## 3. Computational details

### 3.1. Computational configuration and meshes

The schematic of the DLR supersonic combustor is shown in Fig. 1. Based on the previous work using 3D computational domain with various combustion models [17–24], it has been found that the interactions between the originally 15 circular sonic fuel injectors (each of 1.0 mm in diameter, and evenly-spaced at a distance of 2.4 mm at the strut base along the combustor centerline) are relatively small, and the main flow structures show quasi-two-dimensional characteristics, which are particularly true for the shocks, expansion fans and shear

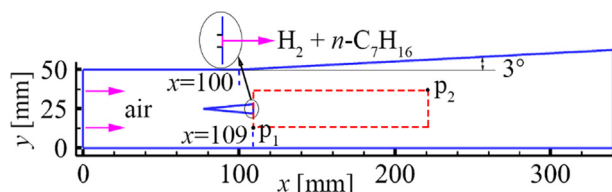


Fig. 1. Schematic of the two-dimensional DLR supersonic combustor [15]. The domain corresponding to the red dashed box  $P_1$ - $P_2$  behind the strut is used for visualizations in Figs. 5, 6, 8, 11 and 13.

layers between central recirculation zone and the high-speed incoming flows. Therefore, the two-dimensional (2D) approximation without considering turbulence-chemistry interaction is widely adopted in the simulations of this combustor [25,26,48,49]. The results from these 2D [25,26,48,49] or quasi-2D (narrow in the third direction with only one or three injectors) [17–24] calculations well reproduce the main flow and combustion characteristics observed from experiments [15], including various zones of the recirculating flames as well as the lift-off distances. We also use the 2D domain with high mesh resolution to investigate the droplet-laden supersonic combustion, which is expected to considerably reduce the computational overhead and hence renders parametric studies affordable.

Moreover, based on a *posterior* comparisons with our previous investigations on this DLR combustor with gaseous  $H_2$  flames using 3D LES with one-equation eddy viscosity turbulence model and Partially Stirred Reactor (PaSR) combustion model [17–19], the 2D simulations in this study reproduce quite well for most features, e.g. temperature, pressure and Mach number, both instantaneously and statistically. The shock waves, expansion fans, and central combustion zones do not show fundamental differences compared qualitatively with those from other 3D works, e.g. by Berglund [20] (three injectors with one-equation flamelet model), Fureby [21] (three injectors with mixed model for turbulence and PaSR model for combustion), Menon [22] (one injector with a localized dynamic closure for turbulence and eddy dissipation concept for combustion), Gong [23] (one injector with one-equation eddy model for turbulence and Eulerian stochastic fields method for combustion), and Li [24] (three injectors with one-equation eddy model for turbulence and PaSR model for combustion). The limitation of 2D simulations mainly lies in the upstream of the recirculation zone (approximately from  $x = 109$  mm to 130 mm), which is highly unsteady due to vortex shedding at the strut base [21,22]. However, the effect of the two-dimensional approximation on the droplet dynamics is limited. No significant dispersion of droplets is seen before  $x \approx 142$  mm as shown later in Fig. 7 and the evaporation rate is relatively low before  $x \approx 130$  mm (see Fig. 9). Hence, the results obtained from 2D approximation in this study would not cause obvious discrepancy with those in 3D simulations for the droplet-laden cases.

In our computational domain in Fig. 1, the combustor is 50 mm in height (i.e.  $y$ -direction) at the entrance and 340 mm in length (i.e.  $x$ -direction) [15]. The upper combustor wall has a divergence angle of  $3^\circ$  since  $x = 100$  mm (indicated in Fig. 1) to compensate for the boundary layer expansion, which also leads to flow asymmetry after the strut as has been widely observed [16–25]. The wedge-shaped strut is 32 mm in length and 6 mm in height. It is placed along the centerline of the combustor at 77 mm downstream to the entrance and the location for the strut base is  $x = 109$  mm. In particular, in the 2D case, the fuel injector at the strut base (i.e. at  $x = 109$  mm) is simplified into a slot (see the elliptical inset of Fig. 1) from the original 15 circular injectors in the experiments, through which the gaseous hydrogen and liquid  $n$ -heptane are injected into the combustor. This similar treatment is also adopted by Wu et al. [26]. To make the global equivalence ratio of  $H_2$  and velocity consistent with the experimental counterparts, the slot width is adjusted to be 0.3 mm.

Three meshes with 55,800, 220,925, and 491,700 structured cells

are generated for grid-dependence analysis (results presented in Section 4.1) and hereafter are denoted as M1, M2, and M3, respectively. Since the zones with combustion and/or strong gas-droplet interaction mostly exist in the downstream region of the combustor after the strut, the grids there are locally refined. The minimum grid size of the three meshes is 0.15 mm, 0.06 mm, and 0.03 mm in  $y$ -direction, and 0.18 mm, 0.14 mm, and 0.10 mm in  $x$ -direction, respectively. The grid resolution of mesh M2 is comparable with the LES work of the same DLR combustor, e.g. by Wang et al. (with a finest resolution of 0.03 mm) [25] and Wu et al. (with an averaged resolution of 0.08 mm) [26]. In their work, the detailed flow and flame structures are predicted reasonably well. Meanwhile, the minimum grid size of mesh M2 are approximately 3 and 7 times larger than the initial droplet diameter (20  $\mu$ m) in  $y$ -direction and  $x$ -direction, respectively. This is expected to be sufficient to predict the source terms (i.e. Eqs. (5)–(8)) in the two-way coupling between the gas phase and the liquid phase and the interpolated gas properties around the droplet surface.

### 3.2. Simulation conditions

Among a series of experimental studies of the DLR combustor with gaseous flames fueled only by  $H_2$  [15], a base case is selected, and its operation conditions of air and  $H_2$  are used in our subsequent studies on supersonic spray flames. The inlet conditions of this case are detailed in Table 2. Specifically, air enters the combustor at  $Ma = 2.0$  with a temperature of 340 K and a pressure of 0.1 MPa, respectively. Hydrogen is injected sonically at a temperature of 250 K and a pressure of 0.1 MPa. The global equivalence ratio of hydrogen for this experimental case is 0.034. The existence of  $H_2O$  in the air stream is due to the vitiated heating of a  $H_2/O_2$  pre-combustion heater used to obtain the desired stagnation temperature of the air inflow [15].

Monodispersed liquid  $n$ -heptane droplets are additionally injected in the foregoing base case (carried by  $H_2$  stream) through the simplified fuel slot (longitudinally at  $x = 109$  mm) as shown in Fig. 1. Eight cases are studied in this work, in which air and hydrogen inlet conditions from the base case (see Table 2), droplet initial properties and injection velocity are kept constant. Hence, the global equivalence ratio of  $H_2$  (here defined as the value without considering  $n$ -heptane) is also kept constant. Specifically, the droplet injection velocity is the same as that of hydrogen, i.e. at 1200 m/s. The initial temperature and diameter of all droplets are assumed to be uniform at 298.15 K and 20  $\mu$ m, respectively. The normal boiling temperature of  $n$ -heptane is 371.65 K. The initial density and heat capacity of  $n$ -heptane are 680 kg/m<sup>3</sup> and 2233 J/kg-K, respectively.

The eight cases shown in Table 3 are differentiated with spray equivalence ratios, which directly leads to the variable initial numbers of droplets in our work. The SER is defined as the global equivalence ratio of  $n$ - $C_7H_{16}/air$  (neglect  $H_2$ ) when the injected liquid droplets are completely vaporized in the combustor. The base case with SER = 0 (i.e. gaseous  $H_2$  flame) is denoted as Case 0 in Table 3, which corresponds to the foregoing experimental base case [15]. For Case 1, the SER is  $\phi_1 = 0.0384$ , whereas for other cases the SERs are gradually increased based on  $\phi_1$  as tabulated in Table 3. When SER >  $2.5\phi_1$ , flame blow-off occurs. Therefore, SER =  $2.5\phi_1$  is regarded as the upper limit of SER for flame stabilization under the studied operating conditions for this supersonic combustor fueled by hydrogen and liquid  $n$ -heptane sprays.

Table 2  
Inflow conditions of air and hydrogen [15].

inlet	$u_x$ [m/s]	$T$ [K]	$p$ [MPa]	$Ma$	$Y_{O_2}$	$Y_{N_2}$	$Y_{H_2O}$	$Y_{H_2}$
air	730	340	0.1	2.0	0.232	0.736	0.032	0.0
hydrogen	1200	250	0.1	1.0	0.0	0.0	0.0	1.0

**Table 3**  
Global spray equivalence ratios of *n*-heptane in Cases 0–7.

Case #	0	1	2	3	4	5	6	7
SER	0	$\phi_1^*$	$1.25\phi_1$	$1.5\phi_1$	$1.75\phi_1$	$2.0\phi_1$	$2.25\phi_1$	$2.5\phi_1$

\* The global spray equivalence ratio  $\phi_1$  in Case 1 is 0.0384.

## 4. Results and discussion

### 4.1. Mesh sensitivity analysis and model validation

Fig. 2 shows the distributions of time-averaged axial velocity at different cross-sections for the non-reactive case (the operating conditions tabulated in Table 2, but with combustion deactivated). They are computed with three meshes, i.e. M1, M2 and M3. Meshes M2 and M3 give similar results, and both are better than those with mesh M1. This is particularly true in the strut wake zone as shown in  $x = 120$  mm, indicating the insufficient grid resolution of mesh M1 in the wake.

Fig. 3 shows the profiles of time-averaged axial velocity and temperature with meshes M1, M2 and M3 at three spanwise locations for the reactive case (i.e. Case 0 in Table 3). Overall, the results from meshes M2 and M3 are closer to the experimental data than those from M1 in most shown locations. The overshoot of the computed axial velocity behind the strut at  $x = 120$  and 167 mm is also seen in the LES work with detailed chemistry, e.g. in Refs. [20,22,23,38]. The temperature over-predictions behind the strut at  $x = 120$  and 167 mm can be attributed to the one-step chemistry for hydrogen oxidation (mentioned in Section 2.3). Overall, mesh M2 is acceptable in terms of computational accuracy and speed, and hence is used for the following analyses on the two-phase supersonic flames.

To validate the droplet evaporation model presented in Section 2.2, we simulate the evaporation process of a single *n*-C<sub>7</sub>H<sub>16</sub> droplet in an inert environment filling with nitrogen. The initial pressure and temperature of the environmental nitrogen are 0.1 MPa and 973.15 K, respectively. The gas temperature is kept nearly constant using a hot furnace, whereas the gas pressure may change slightly with evaporation of the droplet in the experiment [50]. The initial droplet diameter is  $d_0 = 1.285$  mm. Four cases differentiated with initial slip velocity between the gas and droplet ( $U_{slip}$ ) are simulated, which are detailed in Table 4. Case C1 with  $U_{slip} = 0$  m/s is the experimental case. In Cases C2–C4, the slip velocity decays naturally due to drag force, and hence, their evaporation profiles do not show strict linearity but decrease with the decrease of  $U_{slip}$ . Fig. 4(a) shows the comparisons of the temporal evolution of the square of *n*-heptane droplet diameter between the numerical results and experimental data [50]. The averaged relative error ( $\epsilon_e$ ) of the evaporation coefficient  $C_v$  (in mm<sup>2</sup>/s, the dashed lines) to the experimental value for each case is indicated in Fig. 4(a) as well.

The numerical prediction of  $d^2$  in Case C1 in Fig. 4(a) well reproduces the initial increase of the droplet diameter. This period is the heat-up process of the droplet due to thermal conduction from gas, which leads to droplet thermal expansion [50]. For the second stage, linear variations of  $d^2$  with respect to time is captured in Case C1, but the slope magnitude, i.e.  $C_v$ , is under-calculated (about 31%) than the experimental data. This difference may be caused by three major sources of error in the measurements, which however are not considered in the numerical simulations. The first two are the heat conduction from the quartz fiber holding the vaporizing droplet and the radiative heat transfer from the walls of the experimental facilities [50]. A combination of heat conduction through the fiber and radiative effect can decrease the lifetime of the droplet by about 15% for the specific case of using *n*-heptane droplet in a nitrogen-filled environment at 773.15 K and 3.0 MPa [50]. The third one is the free falling of the hot furnace in the experiment, which may cause gas turbulence in the enclosed test facility and relative motion between the gas and droplet. This may remarkably increase the evaporation rate as demonstrated in

Fig. 4(a). Hence, under-estimation of single droplet evaporation especially at high temperatures may be due to the above three major factors, which would enhance the droplet evaporation rate in the experiments but are not considered in the numerical simulations.

Based on Fig. 4(b) (the initial pressure of environmental nitrogen is 0.1 MPa and the initial droplet diameter is 1.285 mm, respectively), when the initial temperature of the gas phase is decreased, the agreements are improved (see the relative errors indicated in Fig. 4b). In general, the evaporation model detailed in Section 2.2 can predict the droplet evaporation with reasonable accuracy under different gas and droplet conditions. Furthermore, the three major error sources except the radiative heat transfer does not exist in the simulations of the DLR combustor. The relative error of the evaporation model is expected to be minimized to that at lower temperatures, e.g. 7.9% at 673.15 K and 7.3% at 773.15 K.

### 4.2. Phenomenological analysis of flow and flame behaviors under two-phase conditions

Fig. 5 shows the contours of instantaneous gas phase axial velocity for Cases 0–7. Overall, the regions with relatively low and even negative axial velocities (corresponding to the recirculation zones and the blue regions beyond them) are longitudinally lengthened from Case 0 to 7 with increased SER. Meanwhile, those regions also become radially broader with larger SER. With droplet injection, the gas axial velocity is positive along the centerline, and the recirculating zone becomes disconnected. This RZ disconnection phenomenon is not found in the droplet-free case, Case 0, and may result from the momentum exchange between the high-speed injected droplets and the surrounding gas in the RZ. Furthermore, based on the time-averaged axial gas velocity fields (not shown here), the maximum mean RZ lengths are about 50 mm off the rear of the strut (i.e. approximately 160 mm in Fig. 5) in all the simulated two-phase cases, which is close to that of Case 0. This implies that the addition of the droplets has small influences on the mean RZ length. Nevertheless, the low-speed zones (i.e. the dark blue regions in Fig. 5) are lengthened in the streamwise direction with increased SER, which indicates the considerable reduction of the local Mach number in the combustor center. This may considerably enhance the mass and heat exchange between the gas phase and droplet phase, which may cause local cold bubbles (see Fig. 6) and increase the probability of local flame extinction.

Likewise, Fig. 6 shows the contours of instantaneous gas phase temperature for Cases 0–7. The maximum RZ lengths are denoted by the red line (i.e.  $x \approx 160$  mm). Compared to that of Case 0, the temperature of the recirculation zones in Cases 1–4 considerably decreases due to the presence of liquid *n*-heptane droplets (see some locations in Fig. 6 indicated by the white arrows). This can be attributed to the droplet evaporative cooling and convective heat transfer between the

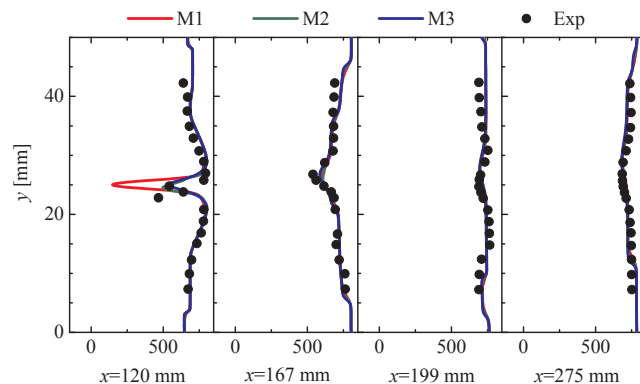


**Fig. 2.** Comparisons of time-averaged axial velocity (in m/s) for Case 0 with combustion deactivated with the experimental data [15].

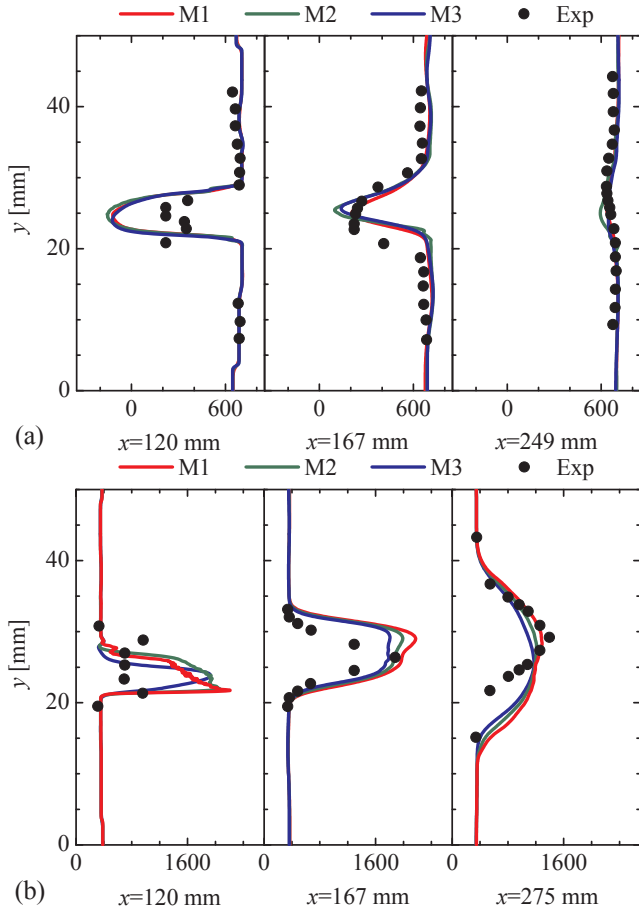


Fig. 3. Comparisons of time-averaged (a) axial velocity (in m/s) and (b) temperature (in K) for Case 0 with combustion activated with the experimental data [15].

Table 4  
Initial slip velocities between the gas and droplet in Cases C1–C4.

Case #	C1	C2	C3	C4
$U_{slip}$ [m/s]	0	1	2	5

two phases. However, with further increased SER (say Cases 5–7), close to the strut, two pronounced branches of the flame base with similar gas temperature are observable, different from the single-side high-temperature zone in, e.g. Case 0. Their effects on flame stabilization are further discussed in Section 4.5. As mentioned earlier, higher SER corresponds to more droplets injected and the availability of more  $n$ -

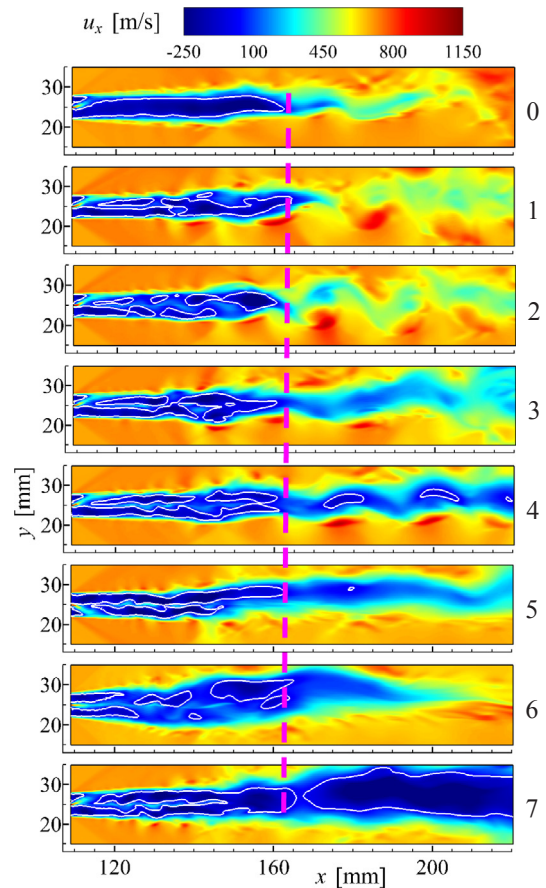


Fig. 5. Contours of instantaneous gas phase axial velocity for Cases 0–7 (labelled by the numbers). The domain corresponds to the red dashed box  $P_1$ – $P_2$  behind the strut. The iso-lines indicate zero gas phase axial velocity (i.e.  $u_x = 0$  m/s).

heptane vapor vaporized from the liquid phase, and therefore more heat can be released from the dual fuel combustion process, which dominates the foregoing cooling effects in these scenarios. Beyond the recirculation zone ( $x > 160$  mm), in Cases 1–3, the peak temperature (i.e. over 2500 K) becomes higher than that of the gaseous  $H_2$  flame, Case 0. Moreover, as SER increases (e.g. Cases 4–7), the hot regions are more extensive, although the peak temperature distributions are more localized. This can justify the expansion of the low-speed region of the corresponding cases as shown in Fig. 5. Expanded hot regions towards the combustor exit may finally lead to thermal choking of the combustor [51], which should be avoided practically to prevent the deterioration of the scramjet overall performance and even sudden misfire during operational mode.

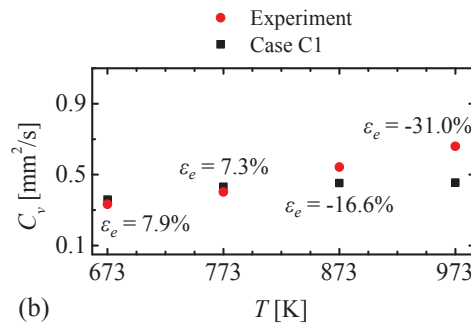
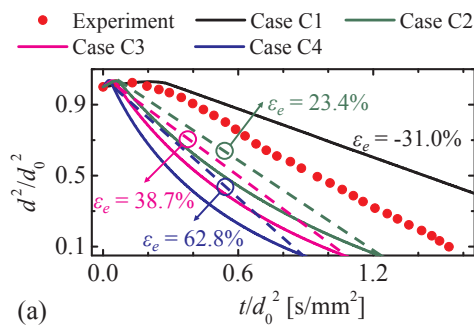


Fig. 4. Comparisons with the experimental data [50] about (a) the temporal variation of the square of droplet diameter and (b) evaporation rate constant under different initial temperatures.

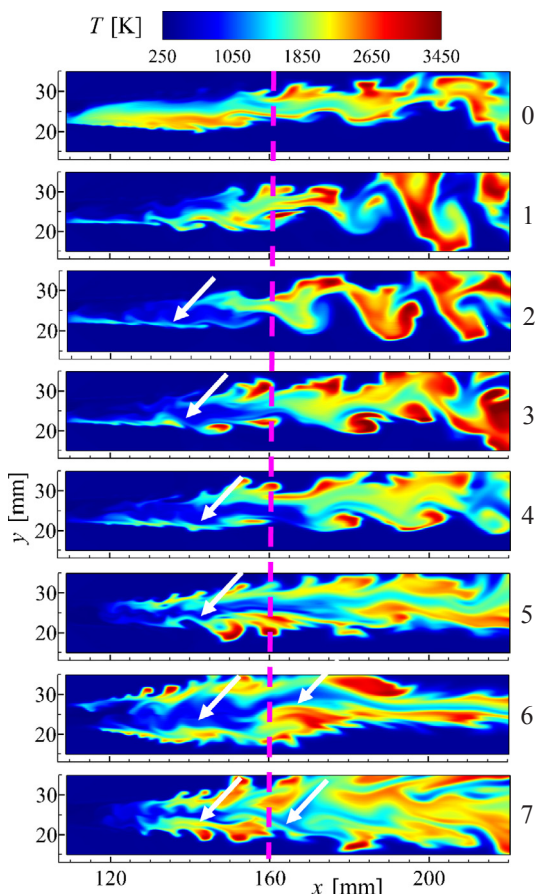


Fig. 6. Contours of instantaneous gas phase temperature for Cases 0–7 (labelled by the numbers). The domain corresponds to the red dashed box  $P_1$ – $P_2$  behind the strut. The red line indicates the approximate streamwise location ( $x \approx 160$  mm) of the recirculation zones.

### 4.3. Droplet evaporation

The typical instantaneous distribution of the liquid *n*-heptane droplets from Case 1 are presented in Fig. 7(a) and the background contour denotes the instantaneous mass fraction of the *n*-heptane vapor in gas phase. After the droplets are injected from the base of the wedge-shaped strut (i.e.  $x = 109$  mm), limited dispersions are observed due to the high droplet velocity (i.e. 1200 m/s) and therefore their diameters change little (close to the initial size, i.e. 20  $\mu$ m). Visually, these droplets form a straight red line approximately from  $x = 109$  mm to  $x = 142$  mm, which is indicated as the main droplet stream in Fig. 7(b). Nevertheless, around the downstream edge of the RZ (for clarity, its streamwise location is denoted by the vertical dash-dotted white lines in both Fig. 7a and b), the diameters show considerable variations, ranging from its initial values to small ones close to zero. This implies that significant droplet evaporation occurs there. Meanwhile, the velocities of the droplets near RZ edge (dash-dotted lines) are relatively low due to the stagnant gas velocity fields there. The details in this region are further enlarged in Fig. 7(b). Besides the main droplet stream from the injector (as indicated in Fig. 7), large amount of the dispersed droplets is observable, which are caused by the local recirculating flows. Some of them are trapped in the RZ, which have long residence time (as long as 0.38 ms, which is much longer than the droplet nominal flow-through time in the RZ, i.e. 0.034 ms) and continuously vaporize with boiling temperature (371.65 K), thereby leading to high *n*-heptane concentrations in the downstream of the hot recirculation zone (see Fig. 7b). However, these dispersed droplets cannot be transported towards more upstream locations, since most of them have been fully evaporated about around  $x = 130$  mm. In addition, based on Fig. 7(a), considerable droplets can penetrate through the RZ due to their high velocity, and are seen downstream beyond the RZ. Their diameters continuously decrease due to the evaporation. However, the local mass fraction of *n*-heptane vapor is much smaller than that in the RZ due to the combustion there.

The spatial distributions of time-averaged *n*-heptane vapor mass fraction for Cases 1–7 are shown in Fig. 8. As SER increases, the lengths of the zones with considerable mass fraction of vaporized *n*-heptane gas are monotonically increased, indicated by Line A in Fig. 8. In Case 1,

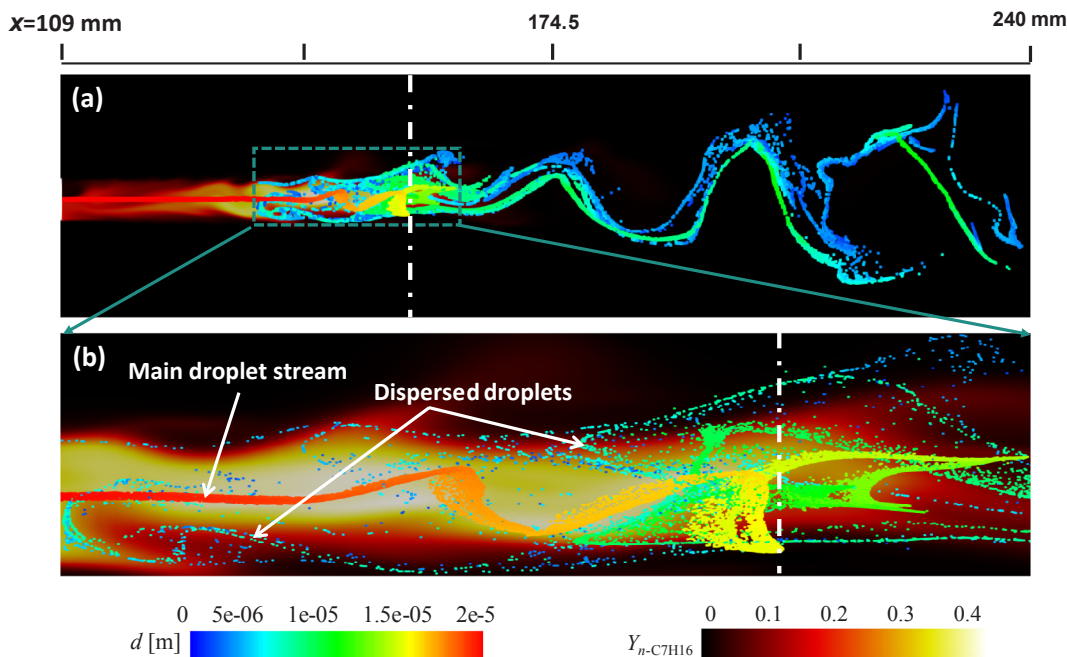
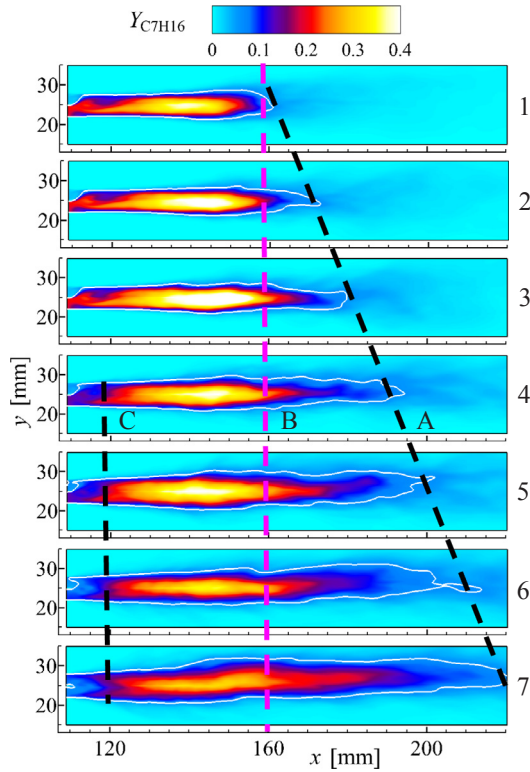
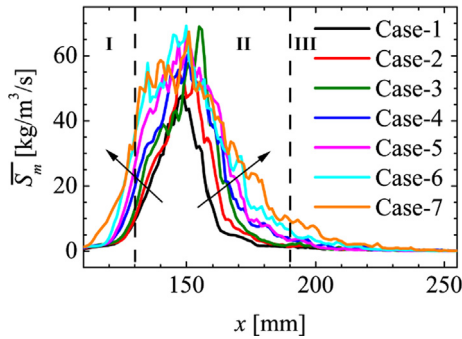


Fig. 7. (a) Instantaneous *n*-C<sub>7</sub>H<sub>16</sub> mass fraction with droplet distribution from Case 1, and (b) The enlarged domain indicated with the green dashed box in (a). The droplets are colored by their respective diameters. The dash-dotted lines in (a) and (b) denote the averaged maximum streamwise location of the recirculation zone.



**Fig. 8.** Contours of time-averaged mass fraction of *n*-heptane vapor for Cases 1–7. Line A indicates the maximum time-averaged streamwise distance of stoichiometric *n*-heptane vapor, Line B for that of recirculation zones, Line C for that of finite *n*-heptane vapor mass fraction.



**Fig. 9.** Longitudinal profiles of averaged droplet evaporation rates for Cases 1–7. The starting point of *x*-axis lie at the rear edge of the strut (i.e.  $x = 109$  mm). I: reaction induction zone; II: transitional zone; III: the fully developed zone.

the RZ is almost full of *n*-C<sub>7</sub>H<sub>16</sub> gas, due to the local evaporation and also the transport by the recirculating flows, as we discuss in Fig. 7. More and more *n*-C<sub>7</sub>H<sub>16</sub> gas is seen beyond the RZs (loosely denoted by Line B in Fig. 8) behind the strut wake from Case 2 to Case 7. In Cases 1–3, the peak *n*-C<sub>7</sub>H<sub>16</sub> mass fractions increase (exceed 40% in Cases 2 and 3), whilst since Case 4, the peak gradually decreases due to the increased SER. Furthermore, in Cases 4–7, the *n*-heptane vapor exists at a distance downstream the strut, as denoted with Line C in Fig. 8.

The spatial availability of *n*-heptane vapor is directly affected by the local droplet evaporation rate in the combustor. To quantitatively compare the evaporation rates in the different cases, the averaged evaporation rate  $\bar{S}_m$ , is introduced

$$\bar{S}_m = \int_{L_y} S_m dy / \int_{L_y} dy, \quad (25)$$

where  $L_y$  is the distance along *y*-direction of the DLR combustor. It is a

measure of the evaporation rate per unit cell volume on a certain plane normal to the streamwise direction in the DLR combustor. Fig. 9 shows the averaged evaporation rate along the streamwise direction (*x*-direction) for the seven cases. Two dashed lines correspond to the boundaries of the reaction induction zone (Zone I in Fig. 9), the transitional zone (Zone II), and the fully developed zone (Zone III), which are found from the earlier modelling work on gaseous H<sub>2</sub> flames in this combustor [17,21]. Generally,  $\bar{S}_m$  is initially small, and then increases rapidly in Zone I. The peak values for all cases are present in Zone II, which locates around  $x = 150$  mm. This location is close to the stagnation point of the RZ and also the intersection points of the two wall-reflected shocks and the shear layers. Therefore, in Zone II the droplet evaporation is considerably facilitated. The evaporation is almost finished in Zone III. Furthermore, the distributions of  $\bar{S}_m$  get longitudinally broader with increased SER. Therefore, from the viewpoint of liquid fuel efficient utilization, the injection scheme in a supersonic combustor should be carefully designed in order to have optimal evaporation process. For instance, one can inject LHCF at several separated locations (e.g. at the strut base, on the combustor walls [52,53]), shift the injection of LHCF towards upstream at high SERs [54,55].

#### 4.4. Mixing and combustion characteristics of dual-fuel supersonic flames

To study the reactant mixing in this three-stream system (H<sub>2</sub>/*n*-C<sub>7</sub>H<sub>16</sub>/air), two mixture fractions,  $\xi_1$  and  $\xi_2$ , are introduced respectively:

$$\xi_1 = Y_{H_2} + Y_{C_7H_{16}} + \frac{2W_H}{2W_H + W_O} \cdot Y_{H_2O} + \frac{W_C}{W_C + 2W_O} \cdot Y_{CO_2} - \frac{2W_H}{2W_H + W_O} \cdot \frac{Y_{H_2O}^0}{Y_{N_2}^0} \cdot Y_{N_2}, \quad (26)$$

$$\xi_2 = \frac{\frac{W_C}{W_C + 2W_O} \cdot Y_{CO_2} + \frac{7W_C}{7W_C + 16W_H} \cdot Y_{C_7H_{16}}}{\frac{7W_C}{7W_C + 16W_H} \cdot \left( Y_{H_2} + Y_{C_7H_{16}} + \frac{2W_H}{2W_H + W_O} \cdot Y_{H_2O} + \frac{W_C}{W_C + 2W_O} \cdot Y_{CO_2} \right)}, \quad (27)$$

where  $W_i$  is the molecular weight of element *i* (i.e. C, H, N and O),  $Y_{H_2O}^0$  and  $Y_{N_2}^0$  are the mass fractions of H<sub>2</sub>O and N<sub>2</sub> in the air stream, respectively. It is obvious that for the air stream,  $\xi_1 = 0$ ,  $\xi_2 = 0$ ; for the hydrogen stream,  $\xi_1 = 1$ ,  $\xi_2 = 0$ ; and for the *n*-heptane stream,  $\xi_1 = 1$ ,  $\xi_2 = 1$ . It means that  $\xi_1$  ranges from 0 in the oxidizer stream to 1 in the fuel stream, while  $\xi_2$  ranges from 0 if the fuel originates only from the hydrogen stream to 1 if the fuel originates only from the *n*-heptane stream for every composition  $\xi_1$ . Therefore, the parameter set  $\xi_1 - \xi_2$  can describe every possible composition in the local mixture.

Fig. 10 shows the scatter plots of  $\xi_2$  versus  $\xi_1$  for Cases 1, 3, 5, and 7. For the full range of  $\xi_1$  in the shown cases, significant stratified combustion characteristics are presented and various compositions of fuels are available with  $\xi_2$  roughly being from 0 to 0.9. The fact that the  $\xi_2$  cannot reach 1.0 or 0 means that no local mixtures in the combustor only has H<sub>2</sub> or *n*-C<sub>7</sub>H<sub>16</sub>. The hydrogen-dominant mixtures, parameterized by low  $\xi_2$ , are more difficult to exist with larger SER (like Cases 5 and 7, less scatters below the red lines), especially at the fuel-lean side (i.e. when low  $\xi_1$ ). Moreover, the *n*-heptane-dominant mixtures (high  $\xi_2$ ) are seen from low to moderate  $\xi_1$  (roughly  $0 < \xi_1 < 0.5$ ). It means that the *n*-heptane vapor from droplet evaporation can exist from fuel-lean to fuel-rich mixtures. At fuel-rich side with high  $\xi_1$ , H<sub>2</sub> in the mixture becomes significant, which corresponds to the upstream of the RZ close to the strut base. Furthermore, the lower critical values of  $\xi_2$  corresponding to high temperature regions increase, e.g. which is 0.2 in Cases 1 and 3, whereas 0.4 in Cases 5 and 7. This implies that with increased SER, *n*-heptane combustion may have a more important contribution towards the heat release, thereby leading more high temperature regions in the downstream as indicated in Fig. 6.

Fig. 11 shows the contours of  $\xi_1$  and  $\xi_2$  in physical space for Case 1. It is seen from Fig. 11(a) that  $\xi_1$  is considerable mainly in the RZ (approximately  $x < 160$  mm), indicating the local fuel-rich composition.

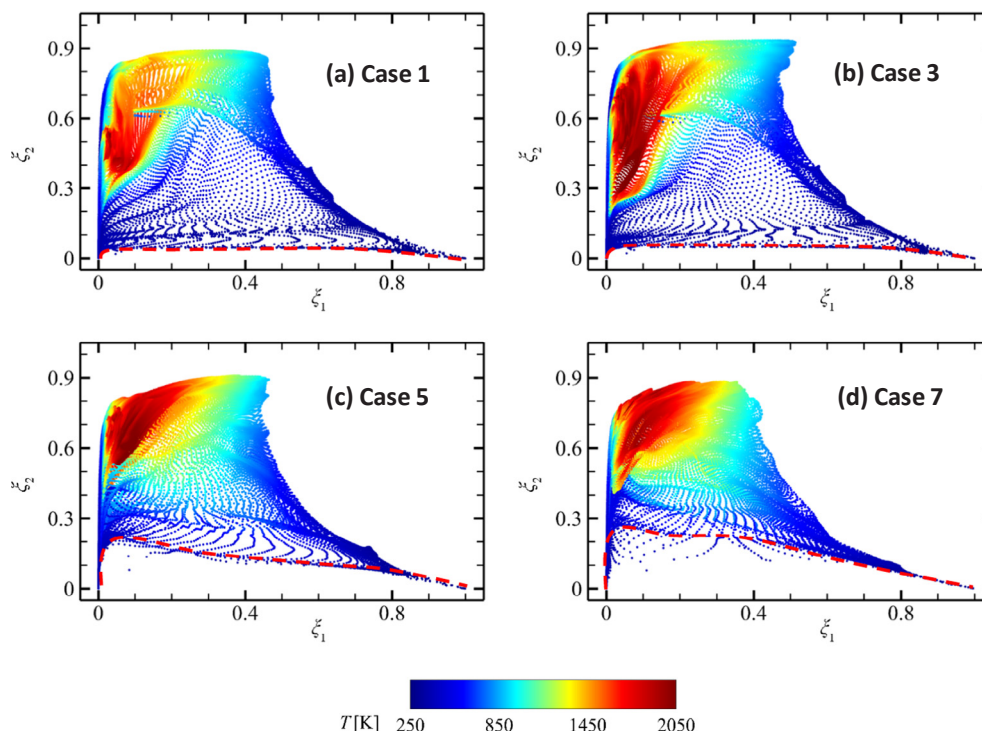


Fig. 10. Scatter plots of  $\xi_2$  versus  $\xi_1$  colored by gas temperature in Cases (a) 1, (b) 3, (c) 5 and (d) 7. The red dashed lines denote the lower range of  $\xi_2$ .

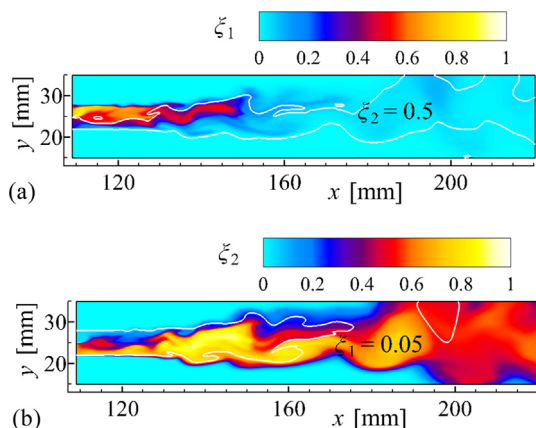


Fig. 11. Contours of (a)  $\xi_1$  with iso-lines of  $\xi_2 = 0.5$  and (b)  $\xi_2$  with iso-lines of  $\xi_1 = 0.05$  for Case 1. Note that  $\xi_2 = 0.5$  denotes the mixture with equal mass mixed  $H_2/n-C_7H_{16}$  while  $\xi_1 = 0.05$  is chosen as a typical intermediate value from  $z_{H_2}^{st} < \xi_1 < z_{n-C_7H_{16}}^{st}$ , where  $z_{H_2}^{st} = 0.0282$  and  $z_{n-C_7H_{16}}^{st} \approx 0.0618$  are the stoichiometric mixture fractions of  $H_2$  and  $n-C_7H_{16}$ , respectively.

This high fuel concentration may result from upstream fuel injection and local droplet evaporation, as well as recirculating flow transport. Beyond the RZ,  $\xi_1$  decays quickly, probably because of the fast mixing with the supersonic oxidizer stream and chemical reactions. In Fig. 11(b), high values of  $\xi_2$  are pervasive from the strut base to the downstream zone. Therefore, in most locations of the combustor,  $n-C_7H_{16}$  is the major fuel compared with  $H_2$  in terms of their respective compositions. Furthermore, a large fraction of  $H_2$  is consumed shortly after injection (e.g. before  $x \approx 130$  mm for Case 1 as indicated in Fig. 11a), while it takes a much longer distance for the liquid droplets to vaporize (beyond the scope  $x = 220$  mm shown in Fig. 11b), mix with the surrounding gas and react. With increased SER, the fuel-rich zone indicated by high values of  $\xi_1$  grows broader transversely and longer longitudinally as the more droplets injected, the higher evaporation rate and the longer distance are encountered for droplet complete evaporation, which has been demonstrated in Fig. 9. Moreover, with

increased SER from Cases 1 to 7, the zone with high values of  $\xi_2$  also grows larger and  $n-C_7H_{16}$  gets more dominant in the  $H_2/n-C_7H_{16}$  dual fuel system.

Fig. 12(a)–(d) shows the scatters of the heat release rate per unit volume ( $dQ$ ) versus  $\xi_1$  for Case 1, 3, 5, and 7, respectively. As a comparison, the results of  $dQ$  versus  $\xi_1$  for droplet-free case 0 is also shown in Fig. 12(e). The stoichiometric mixture fraction of  $H_2$  when neglecting  $n-C_7H_{16}$  in this case is  $z_{H_2}^{st} \approx 0.0282$ , while this value for  $n-C_7H_{16}$  (neglecting the presence of  $H_2$ ) is  $z_{n-C_7H_{16}}^{st} \approx 0.0618$ . Therefore, the stoichiometric mixture fraction ( $z_{DF}^{st}$ ) for this dual-fuel system should range from  $z_{H_2}^{st}$  to  $z_{n-C_7H_{16}}^{st}$ . It is seen that in Cases 1 and 3, almost all the highest values of  $dQ$  correspond to comparatively low  $\xi_2$ , which means that the heat release rate of hydrogen is stronger than that of  $n$ -heptane. However, with increased SER (e.g. Cases 5 and 7 in Fig. 12), the peaks of  $dQ$  are characterized by the intermediate values of  $\xi_2$  (about 0.5) instead, indicating the almost equal contributions from both fuels. Meanwhile, in Cases 5 and 7, at small  $\xi_1$  close to  $z_{H_2}^{st}$ , extra maxima of heat release can be observed with low  $\xi_2$ . This may result from the hydrogen combustion closer to the strut, where droplet evaporation is still limited.

Table 5 presents the averaged heat release rate (temporally averaged and spatially integrated in the domain) of the eight cases. The heat release from hydrogen combustion  $Q_{H_2}$  shows limited variations, due to the fixed mass flow rate. However, with increased SER,  $n$ -heptane induced heat release  $Q_{n-C_7H_{16}}$  increases gradually, and in Cases 5–7, more than 50% of heat release results from the  $n$ -heptane combustion. As mentioned in Section 3.2, SER = 2.5 $\phi_1$  in Case 7 is the limiting condition for stable combustion prior to blow-off. Therefore, the total heat release from Case 7 can be regarded as the maximum under the stable operation mode of this combustor. It is therefore demonstrated that liquid  $n$ -heptane dilute spray flames can be well stabilized with significant heat release in a wide range of spray equivalence ratios under supersonic combustion conditions. This is significant for the practical use of liquid hydrocarbon fuels in hypersonic propulsion systems.

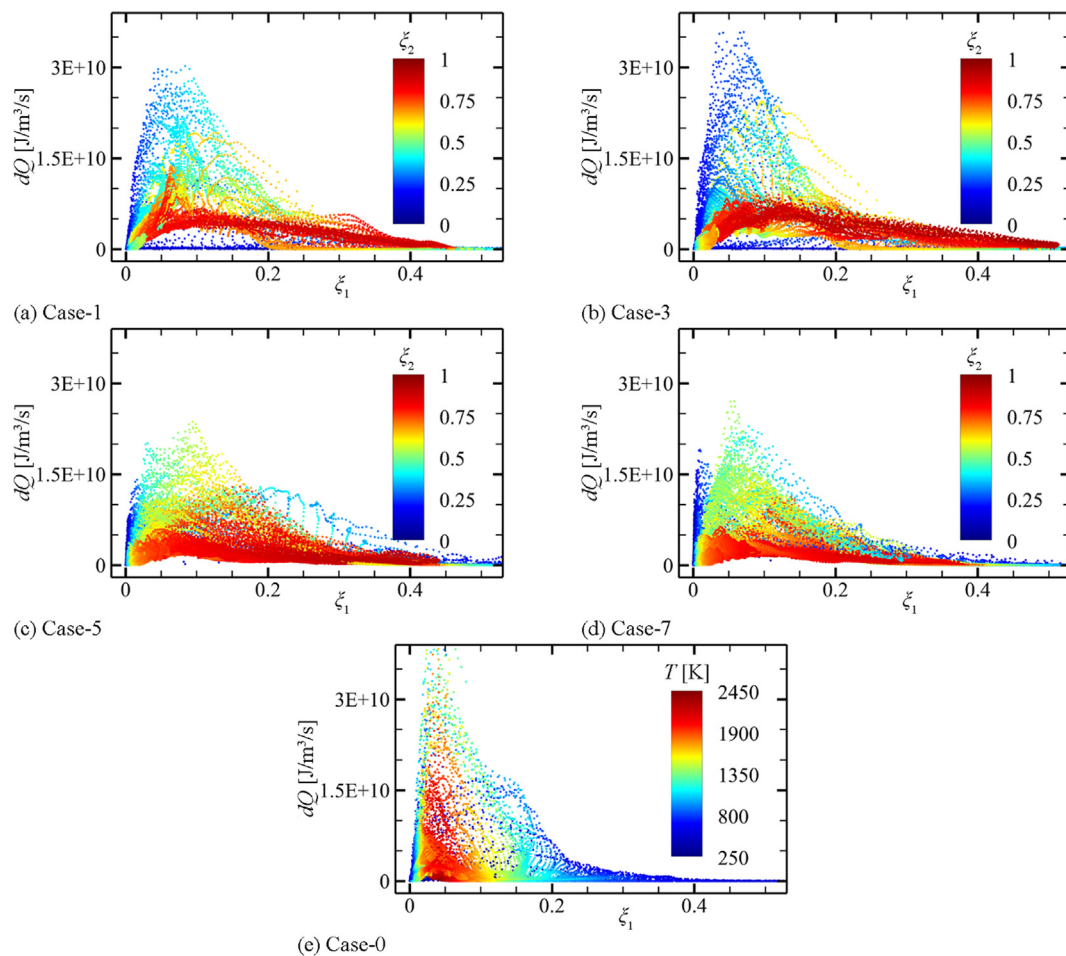


Fig. 12. Scatter plots of  $dQ$  versus  $\xi_1$ . The points are colored by  $\xi_2$  for Case 1, 3, 5, and 7, and colored by temperature for Case 0.

Table 5

Averaged heat release from chemical reactions of hydrogen and *n*-heptane.

Case #	0	1	2	3	4	5	6	7
$Q_{H_2}$ [ $10^4$ J/s]	3.393	3.371	3.497	3.431	3.393	3.395	3.452	3.386
$Q_{n-C_7H_{16}}$ [ $10^4$ J/s]	0	1.772	2.217	2.596	2.918	3.398	3.876	4.437
$f_{n-C_7H_{16}}$ [%]*	0	34.5	38.8	43.1	47.3	50.1	52.9	56.7

\*  $f_{n-C_7H_{16}}$  is the fraction of heat release from *n*-heptane.

#### 4.5. Flame stability analysis

Flame stabilization in supersonic flows is of great importance for practical propulsion systems, which may be influenced by the fuel properties and aerodynamics in the combustor [8,16,26,56]. In the current dual-fuel two-phase system, how the different flames of  $H_2$  and *n*- $C_7H_{16}$  affect the supersonic combustion stability are examined here. Fig. 13(a) and 13(b) show the spatial distributions of the instantaneous reaction rates of  $H_2$  and *n*- $C_7H_{16}$  ( $\dot{\omega}_{H_2}$  and  $\dot{\omega}_{C_7H_{16}}$ ) from Case 1, respectively. It is clearly seen that the reaction zone of  $H_2$  is less spatially extensive than those of *n*- $C_7H_{16}$ . Also, overall, the  $H_2$  reactions occur in the relatively upstream locations. For individual fuels as in Fig. 13(a) or (b), the reaction fronts have two branches, i.e. the upper (arrows 1 and 3 in Fig. 13) and lower (arrows 2 and 4) branches. This asymmetrical distribution of the combustion field may be caused by the  $3^\circ$  expansion of the upper combustor wall since  $x = 100$  mm as indicated in Fig. 1, which also has been widely observed in other works [17–26].

To identify the reaction fronts of individual fuels, the *iso*-surfaces of  $\dot{\omega}_{H_2} = -80$  kg/m<sup>3</sup>/s and  $\dot{\omega}_{C_7H_{16}} = -50$  kg/m<sup>3</sup>/s are used to denote the

$H_2$  and the *n*- $C_7H_{16}$  flame fronts, respectively. Based on our tests, choosing other threshold values of  $\dot{\omega}_{H_2}$  and  $\dot{\omega}_{C_7H_{16}}$ , or other quantities (e.g. gas phase temperature) would not cause obvious change of the identified flame front locations. The locus of the base of flame fronts based on two fuels is defined as the axial location at the first occurrence where the respective fuel reaction rates exceed the foregoing critical values. Accordingly, the flame lift-off distance  $d_{lift}$  is identified as the streamwise distance between the flame base location and the strut base

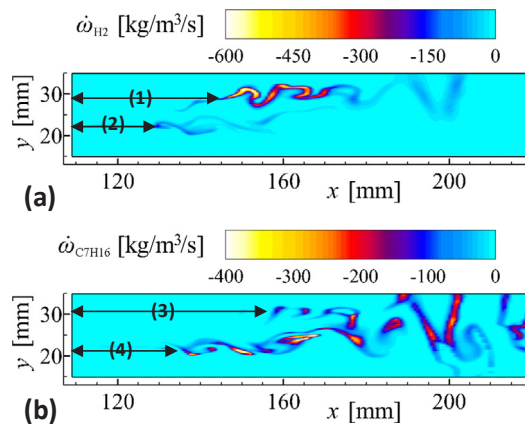


Fig. 13. Instantaneous reaction rates of (a)  $H_2$  and (b) *n*- $C_7H_{16}$  for Case 1. The starting point of *x*-axis lie at the rear edge of the strut (i.e.  $x = 109$  mm). The arrows with numbers 1–4 denote the lift-off distance between the strut and different flame bases.

(i.e.  $x = 109$  mm). Pronounced lift-off behaviors of the reaction fronts can be found based on the results in Fig. 13 for Case 1, which is also seen from the droplet-free Case 0. Based on Fig. 13, in the current  $H_2/n-C_7H_{16}$  system, the upper branches (arrows 1 and 3) are mostly lifted farther off the strut base than the lower ones (arrows 2 and 4). Meanwhile, for the corresponding branches, the upper (lower) branch of  $H_2$  are found to show smaller  $d_{lift}$  than the counterparts of  $n-C_7H_{16}$ . Based on our transient data analysis, the flame base also demonstrates the strong unsteadiness and moves off and approaching the strut base, which was also observed in the other numerical simulation of the same DLR burner [17,26].

Besides Case 1 in Fig. 13, the above flame lift-off characteristics are also observed in other cases. The time-averaged flame lift-off distance  $d_{lift}$  from Cases 0–7 are presented in Fig. 14, which is computed based on the time-averaged reaction rates. Overall, the values of  $d_{lift}$  of  $H_2$  are lower (below 100 mm, which corresponding to  $x = 209$  mm) than those of  $n-C_7H_{16}$ . For larger SER, the  $d_{lift}$  difference between the flame base of two fuels gradually increases, e.g. 150 mm or so for Case 7. It is also interesting to see that with increased SER from Cases 1 to 7, the flame lift-off distance of  $H_2$  generally decreases at the upper branches and increases at the lower branches, which are close to each other in Case 7. However, that of  $n$ -heptane increases at both upper and lower branches from Cases 1 to 7. This indicates that when more liquid droplets are injected, the upper branch of  $H_2$  flame base moves closer to the wedge-shaped strut and therefore stays in the more upstream location of the RZ. Conversely, the  $n-C_7H_{16}$  flames tend to stabilize further downstream. This different behavior of the two flames can be justified by the earlier ignition of  $H_2$  by the hot vitiated recirculating flows from the downstream of the RZ, where stronger  $n-C_7H_{16}$  combustion can be expected due to the availability of more  $n-C_7H_{16}$  vapor with increased SER. Nevertheless, for  $n-C_7H_{16}$  flame stabilization locations, more droplets would also reduce the local temperature because of the evaporative cooling and hence weaken the local  $n-C_7H_{16}$  reactions, thereby lifting the flame farther off the strut. Therefore, the interactions between two reactions fronts play a significant role in flame stabilization of the studied dual-fuel two phase combustor.

Interestingly, the composite of reaction fronts from two fuels also demonstrates novel behaviors about blow-off dynamics. We perform the numerical experiments (results not shown here) based on an instantaneous field with stable combustion from Case 7, through further increasing SER to  $2.75\phi_1$ . In this case, the  $H_2$  flame does not burn stably; instead, it gradually becomes shrinking and localized, and only some islands of  $H_2$  reactions can be found near the strut base (i.e. very upstream in the RZ). Conversely, the  $n$ -heptane reaction zones shrink as well, but gradually transported downstream beyond  $x = 300$  mm, which is close to the exit of our computational domain. Therefore, two reaction zones from  $H_2$  and  $n-C_7H_{16}$  becomes almost disconnected and their interactions are limited, but from time to time some small pockets with hot burned gas are transported from the upstream  $H_2$  reaction zones to stabilize the  $n$ -heptane ones. This transient blow-off process takes finitely long time, i.e. about 2 ms. Ultimate global extinction occurs when the two reaction zones are completely separated. The residual  $H_2$  reactions are quickly quenched, probably due to the local droplets still injected from the fuel slot, whereas  $n-C_7H_{16}$  is extinguished by the insufficient fuel vapor due to reduced evaporation and the cooling caused by the droplets. Therefore, from perspective of blow-off modes, the  $H_2$  flames here blow off like what we observed from other recirculating flames (e.g. in gas turbine flames [57,58]), whereas the  $n$ -heptane ones are fully quenched through lift-off (similar to what is seen from Refs. [59,60] in jet flames). Further systematic numerical studies are desired to understand the blow-off dynamics in two-phase supersonic combustion systems, which is relevant to design and development of practical high-speed propulsion devices.

## 5. Conclusions

Dilute  $n$ -heptane spray flames in a model supersonic combustor originally fueled by hydrogen are studied numerically based on a two-dimensional configuration. Through the grid sensitivity analysis, validations with experimental data, and *a posteriori* comparisons with other three-dimensional simulations on this same combustor [20–24], the two-dimensional approximation can well reproduce most features of the gaseous hydrogen flames, e.g. temperature, pressure, Mach number, shocks, expansion fans and central combustion zones. This may cause an overshoot of axial velocity in the upstream of the recirculation zone, which is highly unsteady short after the strut. However, it would negligibly affect the droplet motion and evaporation due to the high initial velocity of the droplets (1200 m/s). Moreover, the two-phase compressible multi-component reacting system is described by a hybrid Eulerian-Lagrangian method. The emphasis is laid on the effects of  $n$ -heptane spray equivalence ratio on droplet evaporation, reactant mixing and combustion, as well as flame stability.

The varied spray equivalence ratios from 0 to 0.096 before flame blow-off are found to have small influences on the time-averaged length of the recirculation zone behind the strut, which is about 50 mm. However, the low-speed regions in the combustor is increased with them. Meanwhile, the injection of the liquid droplets considerably reduces the gas temperature in the recirculation zone, particularly for small or intermediate spray equivalence ratios, e.g. from 0.0384 to 0.0672. Relatively high evaporation rate of the liquid droplets generally lies in the downstream of the recirculation zone, and continuous evaporation is observable beyond that due to the local high temperature from gas phase combustion.

The mixing field of the dual-fuel system (i.e. liquid  $n$ -heptane and gaseous hydrogen) shows strong inhomogeneity with various compositions of hydrogen/ $n$ -heptane/air mixtures in both mixture fraction space and physical space. The hydrogen-dominant mixture can only exist in the upstream of the recirculation zone (e.g. before  $x \approx 130$  mm for Case 1). However, the  $n$ -heptane-dominant mixture can exist in a much broader range, i.e. from fuel-lean to fuel-rich conditions in mixture fraction space and from upstream to downstream of the combustor in physical space (expands after  $x = 220$  mm for Case 1). The results also show pronounced stratified combustion features due to the inhomogeneous mixing field and distributed droplet evaporation. In addition, the averaged fraction of heat release rate from hydrogen decreases from 100% to 43.3% due to the increased spray equivalence ratio from 0 to 0.096. However, before blow-off the averaged heat release from hydrogen is little affected by the increased spray equivalence ratios, whereas that from  $n$ -heptane increases stably.

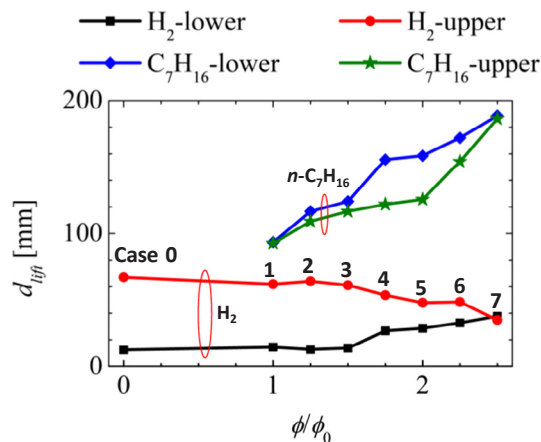


Fig. 14. Time-averaged flame lift-off distance predicted based on  $H_2$  and  $n-C_7H_{16}$  reaction rates with increased spray equivalence ratio. The numbers from 0 to 7 indicate the case indices.

It is also found that the flame stability characteristics are strongly affected by the increased liquid droplet injection conditions. The reaction front base of hydrogen flame moves upstream towards the strut base, whereas that of *n*-heptane is gradually lifted towards the burner exit, when the spray equivalence ratio increases from 0 to 0.096. If it exceeds some critical value (e.g. 0.096 for the current combustor), the flame blows off with the two disconnected reaction zones (upstream hydrogen and downstream *n*-heptane) being fully distinguished. It is demonstrated that the liquid *n*-heptane dilute spray flames can be well stabilized in a wide range of spray equivalence ratios, which is of practical significance for the use of liquid hydrocarbon fuels under supersonic combustion conditions.

#### CRediT authorship contribution statement

**Zhiwei Huang:** Conceptualization, Data curation, Formal analysis, Investigation, Methodology, Resources, Software, Validation, Visualization, Writing - original draft, Writing - review & editing. **Majie Zhao:** Methodology, Software. **Huangwei Zhang:** Formal analysis, Funding acquisition, Methodology, Project administration, Resources, Software, Supervision, Writing - review & editing.

#### Declaration of Competing Interest

The authors declare that they have no known competing financial interests or personal relationships that could have appeared to influence the work reported in this paper.

#### Acknowledgments

This work was financially supported by the start-up grant by National University of Singapore (R-265-000-604-133). The simulations were performed with the computational resources from National Supercomputing Center Singapore (NSCC, <https://www.nsc.sg/>).

#### References

- Ren Z, Wang B, Xiang G, Zhao D, Zheng L. Supersonic spray combustion subject to scramjets: progress and challenges. *Prog Aerosp Sci* 2018.
- Huang Z, He G, Qin F, Cao D, Wei X, Shi L. Large eddy simulation of combustion characteristics in a kerosene fueled rocket-based combined-cycle engine combustor. *Acta Astronaut* 2016;127:326–34.
- Urzay J. Supersonic combustion in air-breathing propulsion systems for hypersonic flight. *Annu Rev Fluid Mech* 2018;50:593–627.
- Segal C. The scramjet engine: processes and characteristics. 2009.
- Kumaran K, Babu V. Mixing and combustion characteristics of kerosene in a model supersonic combustor. *J Propuls Power* 2009.
- Zhang M, Hu Z, He G, Liu P. Large-eddy simulation of kerosene spray combustion in a model scramjet chamber. *Proc Inst Mech Eng Part G J Aerosp Eng* 2010.
- Tian Y, Xiao B, Zhang S, Xing J. Experimental and computational study on combustion performance of a kerosene fueled dual-mode scramjet engine. *Aerosp Sci Technol* 2015.
- Tian Y, Yang S, Le J. Study on flame stabilization of a hydrogen and kerosene fueled combustor. *Aerosp Sci Technol* 2016.
- Nakaya S, Hikichi Y, Nakazawa Y, Sakaki K, Choi M, Tsue M, et al. Ignition and supersonic combustion behavior of liquid ethanol in a scramjet model combustor with cavity flame holder. *Proc Combust Inst* 2015.
- Bao H, Zhou J, Pan Y. The effect of kerosene injection on ignition probability of local ignition in a scramjet combustor. *Acta Astronaut* 2017.
- Li X, Liu W, Pan Y, Yang L, An B, Zhu J. Characterization of kerosene distribution around the ignition cavity in a scramjet combustor. *Acta Astronaut* 2017.
- Xue R, He G, Wei X, Hu C, Tang X, Weng C. Experimental study on combustion modes of a liquid kerosene fueled RBCC combustor. *Fuel* 2017.
- Ren Z, Wang B, Xie Q, Wang D. Thermal auto-ignition in high-speed droplet-laden mixing layers. *Fuel* 2017;191:176–89.
- Ren Z, Wang B, Xiang G, Zheng L. Numerical analysis of wedge-induced oblique detonations in two-phase kerosene-air mixtures. *Proc Combust Inst* 2019;37:3627–35.
- Waidmann W, Alff F, Böhm M, Brummund U, Clauß W, Oswald M. Supersonic combustion of hydrogen/air in a scramjet combustion chamber. *Sp Technol* 1995.
- Qin F, Huang Z, He G, Wang S, Wei X, Liu B. Flame stabilization mechanism study in a hydrogen-fueled model supersonic combustor under different air inflow conditions. *Int J Hydrogen Energy* 2017;42:21360–70.
- Huang Z, He G, Wang S, Qin F, Wei X, Shi L. Simulations of combustion oscillation and flame dynamics in a strut-based supersonic combustor. *Int J Hydrogen Energy* 2017;42:8278–87.
- Qin F, Huang Z, He G, Wang S, Wei X, Liu B. Flame stabilization mechanism study in a hydrogen-fueled model supersonic combustor under different air inflow conditions. *Int J Hydrogen Energy* 2017;42:21360–70.
- Huang Z, He G, Qin F, Wei X. Large eddy simulation of flame structure and combustion mode in a hydrogen fueled supersonic combustor. *Int J Hydrogen Energy* 2015;40:9815–24.
- Berglund M, Fureby C. LES of supersonic combustion in a scramjet engine model. *Proc Combust Inst* 2007;31(2):2497–504.
- Fureby C, Fedina E, Tegnér J. A computational study of supersonic combustion behind a wedge-shaped flameholder. *Shock Waves* 2014;24:41–50.
- Génin F, Menon S. Simulation of turbulent mixing behind a strut injector in supersonic flow. *AIAA J* 2010;48:526–39.
- Gong C, Jangi M, Bai XS, Liang JH, Sun MB. Large eddy simulation of hydrogen combustion in supersonic flows using an Eulerian stochastic fields method. *Int J Hydrogen Energy* 2017;42:1264–75.
- Qing L, Zhenguo W. Dynamic mode decomposition of turbulent combustion process in DLR scramjet combustor. *J Aerosp Eng* 2017;30:4017034.
- Wang H, Shan F, Piao Y, Hou L, Niu J. IDDES simulation of hydrogen-fueled supersonic combustion using flamelet modeling. *Int J Hydrogen Energy* 2015.
- Wu K, Zhang P, Yao W, Fan X. Computational realization of multiple flame stabilization modes in DLR strut-injection hydrogen supersonic combustor. *Proc Combust Inst* 2019.
- Sirignano WA. Fluid dynamics and transport of droplets and sprays. Cambridge, U.K.: Cambridge University Press; 2010.
- Crowe CT, Sommerfeld M, Tsuji Y. Multiphase flows with droplets and particles. 1998.
- Perry RH, Green DW, Maloney JO. Perry's chemical engineers' handbook. 7th Editio. 1998.
- Bradley RS, FUCHS NABT-E and DG in GM, editors. CHAPTER III - NON-STATIONARY EVAPORATION AND GROWTH OF DROPLETS, Pergamon; 1959, p. 60–7.
- Sazhin SS. Advanced models of fuel droplet heating and evaporation. *Prog Energy Combust Sci* 2006;32:162–214.
- Ranz WE, W. R. Marshall J. Evaporation from Drops, Part I. *Chem Eng Prog* 1952;48:141–6.
- Liu AB, Mather D, Reitz RD. Modeling the effects of drop drag and breakup on fuel sprays. *SAE Tech Pap Ser* 2010;1.
- Westbrook CK, Dryer FL. Simplified reaction mechanisms for the oxidation of hydrocarbon fuels in flames. *Combust Sci Technol* 1981.
- Marinov NM, Pitz WJ, Westbrook CK, Castaldi MJ, Senkan SM. Detailed and global chemical kinetic computations for hydrogen-air mixtures. *Transp Phenom Combust* 1996:118–29.
- Ingenito A, Bruno C. Physics and regimes of supersonic combustion. *AIAA J* 2010;48:515–25.
- Gerlinger P, Nold K, Aigner M. Influence of reaction mechanisms, grid spacing, and inflow conditions on the numerical simulation of lifted supersonic flames. *Int J Numer Methods Fluids* 2010.
- Berglund M, Fedina E, Fureby C, Tegnér J, Sabel'nikov V. Finite rate chemistry large-eddy simulation of self-ignition in supersonic combustion Ramjet. *AIAA J* 2010;48:540–50.
- Seo J, Huh KY. Analysis of combustion regimes and conditional statistics of auto-igniting turbulent *n*-heptane sprays. *Proc Combust Inst* 2011.
- Owston R, Magi V, Abraham J. A numerical study of thermal and chemical effects in interactions of *n*-heptane flames with a single surface. *Combust Flame* 2007.
- Li J, Huang J, Chen X, Zhao D, Shi B, Wei Z, et al. Effects of heat recirculation on combustion characteristics of *n*-heptane in micro combustors. *Appl Therm Eng* 2016.
- Martínez-Ruiz D, Urzay J, Sánchez AL, Liñán A, Williams FA. Dynamics of thermal ignition of spray flames in mixing layers. *J Fluid Mech* 2013;734:387–423.
- Greenshields CJ, Weller HG, Gasparini L, Reese JM. Implementation of semi-discrete, non-staggered central schemes in a colocated, polyhedral, finite volume framework, for high-speed viscous flows. *Int J Numer Methods Fluids* 2010;63:1–21.
- Kurganov A, Tadmor E. New high-resolution central schemes for nonlinear conservation laws and convection-diffusion equations. *J Comput Phys* 2000;160:241–82.
- Kurganov A, Noelle S, Petrova G. Semidiscrete Central-Upwind Schemes for Hyperbolic Conservation Laws and Hamilton–Jacobi Equations. vol. 23. 2001.
- Zhao M, Li J-M, Teo CJ, Khoo BC, Zhang HW. Effects of variable total pressures on instability and extinction of rotating detonation combustion. *Flow Turbul Combust* 2019.
- Dasak H. Error analysis and estimation for the finite volume method with applications to fluid flows. *Fluid Dyn* 1996.
- Kummitha OR, Suneetha L, Pandey KM. Numerical analysis of scramjet combustor with innovative strut and fuel injection techniques. *Int J Hydrogen Energy* 2017.
- Wu K, Zhang P, Yao W, Fan X. Numerical investigation on flame stabilization in DLR hydrogen supersonic combustor with strut injection. *Combust Sci Technol* 2017;189:2154–79.
- Ghassemi H, Baek SW, Khan QS. Experimental study on binary droplet evaporation at elevated pressures and temperatures. *Combust Sci Technol* 2006;178:1031–53.
- Larsson J, Laurence S, Bermejo-Moreno I, Bodart J, Karl S, Vicquelin R. Incipient thermal choking and stable shock-train formation in the heat-release region of a scramjet combustor. Part II: large eddy simulations. *Combust Flame* 2015;162:907–20.

- [52] Förster FJ, Dröske NC, Bühler MN, von Wolfersdorf J, Weigand B. Analysis of flame characteristics in a scramjet combustor with staged fuel injection using common path focusing schlieren and flame visualization. *Combust Flame* 2016.
- [53] Liu C, Wang Z, Sun M, Wang H, Li P, Yu J. Characteristics of the hydrogen jet combustion through multipoint injector arrays in a scramjet combustor. *Int J Hydrogen Energy* 2018.
- [54] Huang W. Mixing enhancement strategies and their mechanisms in supersonic flows: a brief review. *Acta Astronaut* 2018;145:492–500.
- [55] Chang J, Zhang J, Bao W, Yu D. Research progress on strut-equipped supersonic combustors for scramjet application. *Prog Aerosp Sci* 2018;103:1–30.
- [56] Zhang J, Chang J, Ma J, Zhang C, Bao W. Investigation of flame establishment and stabilization mechanism in a kerosene fueled supersonic combustor equipped with a thin strut. *Aerosp Sci Technol* 2017;70:152–60.
- [57] Zhang H, Mastorakos E. Prediction of global extinction conditions and dynamics in swirling non-premixed flames using LES/CMC modelling. *Flow, Turbul Combust* 2016;96:863–89.
- [58] Cavaliere DE, Kariuki J, Mastorakos E. A comparison of the blow-off behaviour of swirl-stabilized premixed, non-premixed and spray flames. *Flow, Turbul Combust* 2013;91:347–72.
- [59] Wu CY, Chao YC, Cheng TS, Li YH, Lee KY, Yuan T. The blowout mechanism of turbulent jet diffusion flames. *Combust Flame* 2006;145:481–94.
- [60] Driscoll JF, Donbar JM. Blowout stability limits of a hydrogen jet flame in a supersonic, heated, coflowing air stream. *Combust Sci Technol* 1994;97:137–56.